ELSEVIER

International Journal of Heat and Fluid Flow 23 (2002) 1–12

International Journal of HEAT AND FLUID FLOW

www.elsevier.com/locate/ijhff

Investigation of the cylinder separated shear-layer physics by large-eddy simulation

Stephen A. Jordan

Naval Undersea Warfare Center, Code 74, Building 1346/4, Newport, RI 02841, USA

Received 1 May 2001; accepted 16 August 2001

Abstract

The transition process to turbulence occurring within the separated shear layers of a circular cylinder is investigated by the large-eddy simulation methodology. The Reynolds number ($Re = 8000$) is sub-critical, meaning that upstream separation is laminar. In this study, we desire to improve our understanding of the shear-layer properties as well as assess the capability of the solution methodology to accurately resolve the fundamental characteristics. In the computation, the dynamic eddy-viscosity model is implemented to handle the turbulent scales cut off by the grid-filter. However, the grid-scale level within the shear layer resolves the majority of turbulent scales of interest. The governing equations are re-cast into a curvilinear coordinate framework to accommodate a non-orthogonal grid comprised of line clustering near the cylinder periphery and within the shear-layer region. Two fundamental frequencies persist throughout the entire transition process; one identifying von Kármán shedding and the other denoting the Bloor "transition wave". Only two other mixed modes are clearly discernible. Transition begins approximately 1/4 diameters from separation and concludes about one diameter further downstream. All the characteristic trends of the shear layer, in terms of their growth rate and dependence on *Re*, that were established by M.F. Unal, D. Rockwell [J. Fluid Mech. 190 (1988) 491] have been verified by the present simulation to the higher *Re*. Published by Elsevier Science Inc.

1. Introduction

At Reynolds numbers below critical, laminar separation of the upstream boundary layer along the cylinder surface creates an immediate wake where the flow organizes to form the well-known von Kármán vortex street. This formation region has been studied for over a century beginning with the discovery of Strouhal (1878). As sketched in Fig. 1, the transverse limits of the formation region comprise periodic upper and lower free-shear layers. Both shear layers lie between the point of separation and the initial formation of the large-scale Kármán vortices. Typically, these vortices scale on the order of the cylinder diameter. Most of the phenomena accounting for the Kármán vortex formations originate within the shear layers with the fluctuating rear base pressure contributing to the balance of influence. According to a comprehensive review of recent studies by Williamson (1995), much is understood about the complexity of the shear-layer physics at sub-critical low Reynolds numbers (Re), but by the same token, many questions still remain unanswered, such as their character at moderate and high *Re*.

Our understanding of the cylinder separated shear-layer physics improved significantly due to the experimental investigation by Bloor (1964). She hypothesized that transition from laminar separation to turbulent vortex formation occurs within the separated boundary layer. This process occurs in two phases. Soon after separation, two-dimensional small-scale instabilities arise that amplify into Tollmien–Schlichting waves and eventually lead to turbulence. Due to the three-dimensional nature of the flow within the separated layer, these instabilities experience substantial spanwise distortion, which also contribute to the transition mechanism. Like Bloor (1964), Unal and Rockwell (1988) also found high-frequency disturbances, but only for $Re \geqslant 1900$ and with pronounced amplification at specific tested Reynolds numbers of $Re = 3400$ and $Re = 5040$. At the latter *Re*, they showed that the spectral amplitudes of both the shear-layer velocity fluctuations at the

E-mail address: jordansa@npt.nuwc.navy.mil (S.A. Jordan).

0142-727X/02/$ - see front matter. Published by Elsevier Science Inc.
PII: S0142-727X(01)00134-5

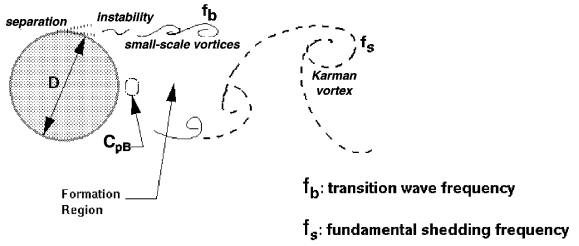

Fig. 1. Sketch of the primary Karman vortex, the initial Bloor instability and the Kelvin–Helmholtz vortices of the circular cylinder near-wake region.

predominant disturbance frequency and the large-scale Kármán vortex at its fundamental frequency vary significantly along the cylinder length.

Early hypotheses refer to the small-scale disturbances as "transition waves". Bloor (1964) detected the appearance of "transition waves" using hot-wire anemometer and reported that the streamwise distance from separation to the initial detection of transition was inversely proportional to the Reynolds number. Her measurements agreed well with the earlier work by Schiller and Linke (1933), who found that the transition point (x_{tr}/D), reference to the mean separation point, decreased from 1.4 to 0.7 as Re increased from 3500 to 8500. At these Reynolds numbers, the Kármán vortices form approximately 2–3 diameters downstream from the cylinder center. Bloor also discovered that the frequencies of the "transition waves" (f_b) normalized by the fundamental shedding frequency of the Kármán vortices (f_s) scale only with the Reynolds number. Specifically, she formularized $f_b/f_s \alpha Re^{\beta}$, where $\beta = 1/2$ over an intermediate range of Reynolds numbers varying between 5.0×10^3 and 2.5×10^4. She justified the 1/2 power-law by assuming that f_b scales with the boundary layer thickness at separation.

Through flow visualization, Wei and Smith (1986) proposed different physics for the separated shear-layer transition process. They observed the creation of Kelvin–Helmholtz (K–H) vortices between separation and the initial large-scale vortex formation (see Fig. 1). These small-scale structures evolve from the same two-dimensional instability mechanism described by Bloor (1964). The Kármán vortices receive the majority of their vorticity from these structures which in-turn originate further upstream from the vorticity contained in the separated boundary layer. One primary difference between the Kármán and shear-layer structures is that the rear base pressure has a minor influence on the K–H vortex formations. In the spanwise direction, the shear-layer vortices distort to periodic cellular structures that align themselves in the streamwise direction. Wei and Smith attributed this alignment to a feedback mechanism delivered from the downstream to upstream structures. At the upper end of the Re intermediate range, the cellular structures become less pronounced and highly irregular.

Although Wei and Smith found the same power-law scaling as Bloor (1964), they reported exponents of $\beta = 0.87$ from their flow visualization results and $\beta = 0.773$ from their hot-wire anemometer measurements. However, Wei and Smith discounted the lower exponent on the premise that the characteristic frequency of the K–H vortices is only captured intermittently by the anemometer signal. Although their higher power-law exponent is nearly twice that of Bloor, they established salient similarities between the "transition wave" hypothesis of Bloor and their K–H vortex phenomena. Wei and Smith argued that the large disparity between the two power-law exponents was attributable to two errors. First, Bloor should scale f_b to the characteristic momentum thickness of the transition region rather than the boundary layer thickness at separation. Secondly, an analysis of her results over the entire range of Reynolds numbers she tested yields a power-law exponent of $\beta = 0.73$, which is close to the value found in their anemometer measurements. In this manner, the results of Bloor are reconciled with Wei and Smith, but in favor of the latter conclusion. Finally, we note that a least-squares fit of the anemometer measurements complied by Prasad and Williamson (1996) of six shear-layer studies (including Bloor and Wei and Smith) show an exponent of $\beta = 0.6742$, which was determined over Reynolds numbers ranging from 1.2×10^3 to 4.5×10^5. They gave a convincing argument for a power-law relationship by noting the variation of the fundamental near-wake characteristics with Re.

Unlike that in free jets and mixing layers (Roshko, 1976; Ho and Huerre, 1984), the small-scale structures inside the separated shear layer of a cylinder do not coalesce. Wei and Smith (1986) did not visualize any pairing of these structures nor did Unal and Rockwell (1988) detect sub-harmonics of the "transition wave" frequency. Conversely, when formation of the Kármán vortex was repressed by Unal (1985) by inserting a downstream splitter plate, streamwise pairing of the K–H vortex structures and the associated sub-harmonics occurred similar to that in a free-shear mixing layer. Besides verifying the existence of "transition wave" frequencies in the shear layers, Unal and Rockwell studied the exponential variation of the maximum and edge velocity fluctuations as well as the integrated kinetic energy at Re ranging from 440 to 5040. These characteristics among others are illustrated in Fig. 2. Unal and Rockwell found the kinetic energy levels to be significantly higher at the fundamental shedding mode compared to the levels at the modes that correlate with the small-scale disturbance. For $Re > 1000$, their measured shear-layer characteristics collapse onto a single growth rate after scaling each by their extrapolated value as obtained upstream at the mean separation

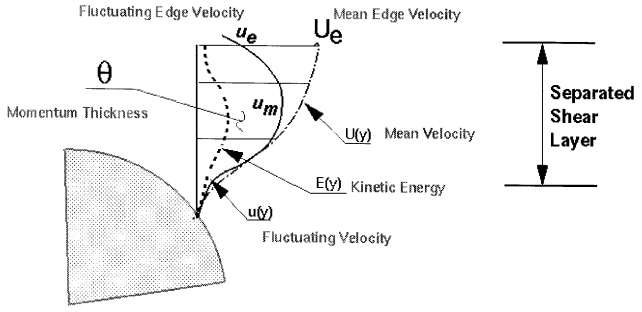

Fig. 2. Separated shear layer characteristics of the circular cylinder.

point. This scaling clearly illustrates the earlier completion of turbulent transition with increasing *Re*, which is easily identified by a zero growth of both the integrated energy and fluctuating streamwise velocities.

There exists an overwhelming number of experimental studies of the cylinder separated shear-layer physics compared to similar numerical investigations. Braza et al. (1990, 1993) reported small-scale instabilities (which they called mixing layer vortices) and pressure–frequency spectra of the cylinder shear layer, but their computations were two-dimensional (2D). Besides obviously ignoring the important spanwise contributions to the streamwise maturity of the K–H vortices, the pressure coefficients near rear stagnation are always over-predicted in two-dimensional simulations of the cylinder wake (Jordan and Ragab, 1998). This latter fact can also arise in three-dimensional computations if the spanwise resolution is inadequate. As a consequence, the formation region of the Kármán vortices is shortened (as well as x_{tr}) and the fundamental shedding frequency is inaccurate. In their computations over *Re* ranging from 2.0×10^3 to 1.0×10^4, Braza et al. (1990) predicted peaks in the pressure spectra of the shear layer at predominant modes of $nf_s \pm mf_b$, where *n* and *m* are integers. However, the number of discrete peaks far exceeded the experimental evidence reported by Kourta et al. (1987). They found discernible sub-harmonics of f_b that disagreed with the experimental measurements of Wei and Smith (1986) and Unal and Rockwell (1988). Additionally, they reported coalescence of the shear-layer vortices prior to formation of the Kármán vortex, which is counter to the flow visualization observations. Their spectral analyses agreed closely with the 1/2 power-law scale of Bloor (1964).

Owing to the lack of novel numerical studies, a large-eddy simulation (LES) was performed to broaden our understanding of the cylinder separated shear-layer physics. One should note that previous LES studies of the cylinder near wake, such as Jordan and Ragab (1998), Ma et al. (2000) and Kravchenko and Moin (2000), focused on the near-wake physics rather that the separated shear layers themselves. The LES methodology easily lends itself to accurate predictions of the salient characteristics of the shear-layer physics because the premise of the approach is to fully resolve the energy-bearing scales of the turbulent field. Specifically, the present shear-layer characteristics were computed at the sub-critical Reynolds number $Re = 8000$ for the following reasons. From a methodology perspective, we want to demonstrate its capability by capturing the true shear-layer physics given sufficient spatial resolution and the proper numerical solution procedure. Additionally, illustrate the appearance of the K–H vortices and their predominant fluctuating modes to ascertain the different exponents as discussed by Wei and Smith (1986). Finally, extend the physics similarity shown by Unal and Rockwell (1988) to a Reynolds number beyond their experimental measurements.

2. Governing equations and numerical method

Recall that the impetus of the present paper is the spatial and temporal resolution of the separated shear layer of the circular cylinder at a sub-critical Reynolds number by the LES methodology. The governing equations are derived by spatially filtering the Navier–Stokes equations along with continuity, which invokes the incompressibility constraint. All turbulent scales removed by the filter process are classified as the sub-grid-scales (SGS). To adequately encompass the near wake with emphasis on resolution of the separated shear layer, a non-orthogonal O-type grid topology was generated. Inasmuch as the spatial resolution is non-uniform throughout the solution domain, the governing equations required transformation to a curvilinear coordinate system (ξ, η, ζ in the streamwise, transverse and spanwise directions, respectively). Consequently, the LES derivation formally involved two spatial operations. Jordan (1999) reasoned that the order of spatial operations is important to ensure, most importantly, that the filter is properly defined. Specifically, transforming the full-resolution equations first (then filter) guarantees that the filter operation is directed along the curvilinear lines. Jordan identified this procedure as the 'alternate approach'. The final form of the governing equations according to the 'alternate approach' appear as

Continuity:

$$\frac{\partial \bar{U}^k}{\partial \xi^k} = 0. \tag{1a}$$

Momentum:

$$\frac{\partial \sqrt{\tilde{g}}\bar{u}_i}{\partial, t} + \frac{\partial \bar{U}^k \bar{u}_i}{\partial \xi^k} = \frac{\partial \sqrt{\tilde{g}}\tilde{\xi}^k_{x_j}\bar{p}}{\partial \xi^k} + \frac{\partial \sigma^k_i}{\partial \xi^k} + \frac{1}{Re}\frac{\partial}{\partial \xi^k}\left[\sqrt{\tilde{g}}\tilde{g}^{k\ell}\frac{\partial \bar{u}_i}{\partial \xi^\ell}\right], \tag{1b}$$

where each term is given in their strong conservative form. The real SGS stress (σ_i^k) in the computational space is defined by both the Cartesian ($\bar{u}, \bar{v}, \bar{w}$) and contravariant ($\bar{U}, \bar{V}, \bar{W}$) velocity components; specifically, $\sigma_i^k = \overline{U^k}\,\overline{u}_i - \overline{U^k u_i}$. The contravariant velocity components in terms of their physical counterparts are evaluated by $\bar{U}^k = \sqrt{\bar{g}}\,\tilde{\xi}^k_{x_j}\bar{u}_j$. Isolating each metric coefficient from the filter operation is permissible because they are considered as smooth second-order-accurate quantities. In these definitions, the overbar denotes the filter operation, and the tilde symbolizes implicit filtering of the metric coefficients ($\tilde{\xi}^k_{x_j}$) and Jacobian ($\sqrt{\tilde{g}}$) through their numerical approximation (Jordan, 1999).

To compute the cylinder shear-layer physics, the above LES curvilinear system was time-advanced in the computational space by a variant of the fractional-step method, which was founded on the development of Kim and Moin (1985). While the second-order implicit Crank–Nicolson scheme was applied to the diffusive terms to eliminate the high viscous stability restriction, the second-order explicit Adams–Bashforth approach was used to time-advance the convective terms. Except for the periodic spanwise components, the convective terms were spatially approximated by third-order-accurate upwind-biased finite differences while the diffusive and SGS terms were discretized using standard second-order-accurate central differences. To capture the small-scale spanwise components, the respective convective derivatives were spatially approximated by a fourth-order compact scheme. All terms in the pressure-Poisson's equation of the fractional-step procedure were central differenced to the second-order with iterations to convergence reached by the modified strongly implicit method. Through extensive application of this fractional-step method, an error tolerance (residual) of 1.0×10^{-4} for the pressure-Poisson equation was found to be sufficient to satisfy the incompressibility constraint. The grid molecule is semi-staggered, meaning that the velocity components are located at the computational points and the pressure variable is computed at the cell centers. Strong coupling between the pressure and the velocity components was maintained using a fourth-order-accurate compact differencing scheme for the pressure gradient at the cell interfaces (Jordan and Ragab, 1996). Globally, the discretization scheme is second-order-accurate in both space and time.

3. Curvilinear form of the dynamic subgrid-scale model

Demarcation between the resolved and modeled turbulent scales in the LES formulation results from the spatial filter operation. For the present computation, we will assume that the respective filter width is synonymous with the grid spacing. Consequently, cut-off of the resolved wavenumbers varies locally due to the non-uniformity of the physical domain resolution. By carefully generating the grid spacing (with some 'a-priori' knowledge of the wake's spectral content), we can ensure that the cut-off wavenumber lies generally within the local energy equilibrium range of the turbulent field. Under this premise, the Leonard and cross terms drop out of the total SGS stress definition and Smagorinsky's turbulent eddy-viscosity relationship (Smagorinsky, 1963) should perform adequately for modeling the real Reynolds stress field. This model is easy to implement and is most common for closing the LES system of equations in practical applications. Smagorinsky's relationship received a welcomed improvement by Germano et al. (1991), who formulated a dynamic evaluation of the model's coefficient. For the present need, this version was re-cast for implementation in the transformed space according to the spatial order-of-operations described by Jordan (2001). As does its Cartesian counterpart, the present dynamic model gives negligible contributions in the inviscid and laminar flow regions of the flow domain as well as the correct asymptotic reduction of the SGS stress when approaching solid walls. As described below, the model's curvilinear coordinate form is equally capable of capturing backscatter of turbulent energy as transferred from the modeled scales to the finest resolved ones across the cut-off wavenumber.

3.1. Smagorinsky's eddy-viscosity relationship

The contravariant form of the dynamic eddy-viscosity modeled for SGS field appears as

$$\sigma_i^k - (1/3)\tilde{\varsigma}^k_{x_j}\tau_{\ell\ell} = 2C\bar{\Delta}^2|\bar{S}|\bar{S}_i^k, \tag{2}$$

where the variable C is considered as the model's coefficient. The filtered metric term $\tilde{\varsigma}^k_{x_j}$ transforms the trace of the Cartesian stress tensor ($\tau_{\ell\ell}$). The turbulent eddy-viscosity (ν_T) is expressed as

$$\nu_T = C\bar{\Delta}^2|\bar{S}|, \tag{3}$$

where $|\bar{S}| = \sqrt{2\bar{S}_{ij}\bar{S}_{ij}}$ is the magnitude of the resolvable strain-rate tensor ($\bar{S}_{ij}$) and $\bar{\Delta}$ is the local filter width. In the physical domain, the non-uniform filter width is defined by $\bar{\Delta} = \sqrt[6]{\tilde{g}} = \sqrt[6]{\tilde{g}_{11}\tilde{g}_{22}\tilde{g}_{33}}$ for orthogonal curvilinear grids. Like the velocity components, the contravariant of the strain-rate tensor ($\bar{S}_i^k$) is defined as $\bar{S}_i^k = \sqrt{\bar{g}}\,\tilde{\xi}^k_{x_j}\bar{S}_{ij}$, where $\bar{S}_{ij}$ is computed along the curvilinear lines in the physical domain using

$$\bar{S}_{ij} = \frac{1}{2\sqrt{\bar{g}}}\left(\frac{\partial\sqrt{\bar{g}}\,\tilde{\xi}^\ell_{x_j}\bar{u}_i}{\partial\xi^\ell} + \frac{\partial\sqrt{\bar{g}}\,\tilde{\xi}^\ell_{x_i}\bar{u}_j}{\partial\xi^\ell}\right). \tag{4}$$

As discussed below, the resolvable strain-rate tensor is cast in a conservative form to eliminate the commutation error that is associated with spatially filtering along non-uniform spacing.

3.2. Dynamic evaluation of the model coefficient

Herein, the derivation of a unique expression for dynamic computation of the model coefficient follows the procedures of Germano et al. (1991) and Lilly (1992) for Cartesian coordinate systems. To start, the grid-scale LES equations are filtered a second time by a test filter with width ($\overline{\overline{\Delta}}_t$) set at twice that of the local grid spacing; $\overline{\overline{\Delta}}_t = 2\bar{\Delta}_g$. Test filtering along the curvilinear lines is easily achieved in either the physical domain or computational space because all required explicit filtering occur after the coordinate transformation operation. If filtering in the non-uniform physical domain is desirable, one can avoid the introduction of the associated second-order error by numerically evaluating each contributing derivative prior to the explicit filter operation. This third spatial operation in the overall derivation produces resolvable tensors similar to their Cartesian counterparts provided that the contravariant velocity components are retained in the process. The modified Reynolds stress (T_i^k) and Leonard stress (L_i^k) in the curvilinear coordinate form of the test-filter LES system become

$$T_i^k = \overline{\overline{u}_i}\overline{\overline{U}}^k - \overline{\overline{u}_i}\overline{\overline{U}}^k, \tag{5a}$$

$$L_i^k = \overline{\overline{u}_i}\overline{\overline{U}}^k - \overline{\overline{u}_i}\overline{\overline{U}}^k, \tag{5b}$$

where the second overbar denotes the test filter operation. Note that both these stress tensors are evaluated along the curvilinear lines by explicitly filtering the Cartesian as well as the contravariant velocity components of the resolved field. The identity derived by Germano (1992) for the Leonard term in Cartesian coordinates has a cognate form in the computational space. That identity is defined by

$$L_i^k = T_i^k - \bar{\sigma}_i^k, \tag{6}$$

where the single overbar denotes the same test filter operator. By assuming that the fine turbulent scales lying between the grid and test filter operations are scale-similar with the SGS, we can justify the same eddy-viscosity relationship for the new modified Reynolds stress. This relationship becomes

$$T_i^k - (1/3)\tilde{\xi}_{x_j}^k T_{\ell\ell} = 2C\overline{\overline{\Delta}}^2 |\overline{\overline{S}}|\overline{\overline{S}}_i^k, \tag{7}$$

where the variable C replicates all turbulent scales removed by the test filter operation. After substituting the definitions for T_i^k and the test-filter SGS stress $\bar{\sigma}_i^k$ into the new identity, the eddy-viscosity relationship for L_i^k becomes

$$L_i^k - (1/3)\tilde{\xi}_{x_j}^k L_{\ell\ell} = 2C\bar{\Delta}^2 M_i^k, \tag{8a}$$

where the model stress field (M_i^k) is defined as

$$M_i^k = \alpha^2 |\overline{\overline{S}}|\overline{\overline{S}}_i^k - \overline{|\bar{S}|\bar{S}_i^k} \tag{8b}$$

with the filter width ratio $\alpha = 2$. A convenient step intrinsic in the L_i^k model derivation is the removal of the model coefficient from the test filter operation. Although this step facilitates the computation, its proper implementation assumes that C is spatially averaged along at least one curvilinear line.

Inasmuch as all terms in Eq. (8a) are resolvable, we can derive a unique dynamic expression for C by employing the appropriate contraction procedure. Lilly (1992) circumvented any singular evaluation of the model coefficient by performing a least-squares minimization of Eq. (8a) that is equivalent to contracting L_i^k with M_i^k. Essentially, the modeled stress field that lies between the grid and test filter scales is assumed to be orthogonal to the respective modified Leonard stress. If we invoke Lilly's approach, we must be careful to insure rotational invariance of C in both the physical domain and transformed space. The proper procedure requires writing the error function in the physical domain before minimizing its square. The contravariant error tensor (E_i^k) along the curvilinear line in the physical domain becomes

$$E_i^k = \sqrt{\bar{\tilde{g}}}\tilde{\xi}_{x_j}^k L_{ij} - (1/3)\tilde{\xi}_{x_j}^k L_{\ell\ell} - 2C\bar{\Delta}^2\sqrt{\bar{\tilde{g}}}\tilde{\xi}_{x_j}^k M_{ij}, \tag{9}$$

where matrices L_{ij} and M_{ij} are not summed independently. Minimizing this error gives the expression

$$C = \frac{L_i^k \cdot M_i^k}{2\bar{\Delta}^2 M_m^k \cdot M_m^k} \tag{10}$$

for the model coefficient, which operates on the inner product of the Cartesian tensor components of L_i^k and M_i^k in the computational space.

Because the dynamic computation of the model coefficient houses matrices dependent on the local instantaneous strain-rates of the resolved field, it can yield both positive and negative values. Physically, positive coefficients denote forward scatter in the turbulent power spectrum, which mirror energy cascading down to the modeled scales. Conversely, the negative values symbolize backscatter, or the reverse of energy from the SGS scales to the finest scales of the resolved field. Unfortunately, experience tells us that the backscatter physics correlate over long execution times, which demand ad hoc measures to guarantee stability. If the solution algorithm is stable under an instantaneous 'zero-viscosity' flow, these physics are permissible up to their equivalent in terms of the molecular viscosity contributions. Otherwise, the best choice for maintaining a stable computation is to truncate all negative contributions from the dynamic model to yield a net zero effect. For the present test case, sufficient resolution of the finer scales was provided within the cylinder shear layer to eliminate all backscatter determinations in the computation.

Recall that explicit filtering of the resolved components can occur in the physical domain or computa-

tional space. Jordan (1999) demonstrated that the resultant damped spectral energy components are identical regardless of the choice, with the difference being only the computational cost. Inasmuch as the partial differentiation and filter operations commute in the transformed space, the test filter should yield equal values for the model coefficient whether it is done before or after evaluating the participating matrices. Conversely, the commutation error associated with the filter operation in the physical domain can only be avoided if the respective matrices (or their first-order components) are computed prior to test filtering. For the present need, the box filter (volume averaging) was exercised to test filter the resolved field. This filter attenuates all Fourier components of the physical quantity except at wavenumber $k = 0$, with a local filter width $2\Delta_{\xi^k}$ along the curvilinear lines. In wavenumber space, the attenuation effects of box filtering are equivalent to a second-order, finite-volume solution methodology of the convective flux vectors along the curvilinear lines.

4. Cylinder shear-layer results and discussion

In this section, we will inspect the LES predictions of the separated shear-layer physics of a circular cylinder at $Re = 8000$ in search of the predominant frequencies, mixed modes and streamwise growth of several fundamental characteristics. Two central issues leading to an accurate LES computation are the prediction of the base pressure coefficient (denoted as C_{pB} in Fig. 1) and the spatial resolution of the streamwise near-wake structures. The former prerequisite is critical to the computation because this parameter strongly correlates with the large-scale vortex formation length, shedding frequency, and spanwise vorticity of the Kármán vortices. The second concern is not only fundamental to the shear-layer oscillations, but also governs the structural content of the K–H vortices and the adjacent formation region.

4.1. Spatial and temporal resolution of the simulation

To satisfy the needs just mentioned, the present computation used the structured grid and flow boundary conditions that were found satisfactory by Jordan and Ragab (1998) for resolving the near-wake turbulence at $Re = 5600$. As shown in Fig. 3, this grid houses $241 \times 241 \times 36$ points in the ξ, η, ζ curvilinear coordinate directions, respectively. The inflow and outflow boundaries were set at 10 and 20 diameters, respectively, and the inner boundary that traces the cylinder surface was no-slip. Along the cylinder periphery, the points were distributed $\Delta s \cong 0.011\pi$ within the upstream laminar boundary layer and $(\Delta s) \cong 0.003\pi$ along the segments that were projected into the shear layer. This

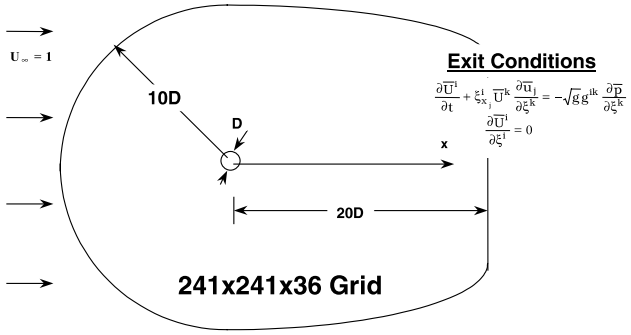

Fig. 3. Geometric and flow conditions for the LES computation of cylinder separated shear-layer.

latter spacing is a slight variation of Jordan and Ragab's original grid because additional spatial resolution was necessary in the shear layer region to accommodate the higher Re. The experimental evidence reported by Mansy et al. (1994) and Williamson et al. (1995) tell us that the spanwise wavelength (λ_z) of the large-scale streamwise eddies scale as $\lambda_z/D \sim 20Re^{-1/2}$. Given 36 spanwise points in the present grid that are equi-distant over length 0.67π, each streamwise eddy was resolved by approximately four points to fourth-order accuracy for its convective component. This resolution compares favorably with the LES computation by Kravchenko and Moin (2000) who used five spanwise points per eddy and second-order accuracy.

A unit velocity condition was applied along the upstream external boundary and Euler's equation (with continuity for closure) was used to cleanly exit the Kármán vortices. Specifically, the continuity equation served to maintain incompressibility along the downstream boundary. The pressure gradient at exit was computed via the velocity update equation of the fractional-step method, which further provided a Neuman boundary condition for the pressure field solution. To close the kinematic definition, periodic end conditions were applied in the spanwise direction.

The present computation began with the last saved solution of Jordan and Ragab (1998). For $Re = 8000$, it was necessary to lower the time step $(\Delta T = 0.0015)$ to maintain a stable computation; $T = tU/D$, where U is the inflow (freestream) velocity. Statistics were not collected until the transient effects that were caused by the higher Re simulation had fully disappeared. Finally, the reader is asked to refer to the publication of Jordan and Ragab (1998) for additional information about the suitability of the grid resolution, and in particular, participation of the SGS model in the overall computation.

Before investigating the shear-layer physics, we will examine several important parameters and properties of the near wake for the primary purpose of justifying the grid resolution and LES solution scheme. These

Table 1
Several predicted global and local characteristics of the cylinder near wake compared to the experimental measurements

Parameter	Computation	Experiment
C_L	0.115	0.12 (Tadrist et al., 1990)
C_D	1.06	1.10 (White, 1974)
S_t	0.204	0.205 ± 0.002 (Norberg, 1993)
ℓ_c	1.69	1.67 (Norberg, 1998)
u'_p	0.46	0.45 (Norberg, 1998)
C_{pB}	−1.08	−1.06 (Williamson, 1995)
f_b/f_s	9.4	10.1 ± 1 (Prasad and Williamson, 1996)
θ_s	92.2	94 ± 2 (Son and Hanratty, 1969)

characteristics are listed in Table 1 along with their respective experimental values. Adequacy of the near-wall resolution can be judged largely by the accuracy of the mean lift amplitude (C_L), drag (C_D) and base pressure coefficients, and the mean separation angle (θ_s). Given sufficient near-wall resolution, the grid spacing further downstream essentially governs the solution accuracy of the shedding frequency, mean formation closure length (ℓ_c), and peak streamwise fluctuation (u'_p). Lastly, proper prediction of the Bloor frequency is regulated by the respective spatial resolution inside the separated shear layer. In the table, the flow parameters C_L, C_D and S_t were extracted from the time history shown in Fig. 4, which illustrate the large-scale shedding process over approximately five cycles. Additionally, each quantity was spatially averaged in the spanwise direction. A comparison between the computed and experimental characteristics shown in Table 1 indicates that each predicted quantity for the present test case is either accurate to be within 5% of the measured value or inside the experimental error.

We can further illustrate the adequacy of the spatial resolution of the separated shear-layer region by examining the root-mean-square (rms) distribution of the fluctuating streamwise velocity (u'_{rms}, scaled by U) and pressure coefficient (C'_p). This rationale is appropriate because these characteristics are statistically self-similar for turbulent wakes at sub-critical Reynolds numbers. Contours of u'_{rms} and C'_p are plotted in Fig. 5 where only the upper half distributions are shown because the turbulent wake is fully symmetric about the cylinder downstream centerline at statistical steady-state. Both distributions closely agree with previously published results for $525 \leqslant Re \leqslant 140,000$ – for example, see Mittal and Balachandar (1996), Jordan and Ragab (1998), and Cantwell and Coles (1983). In particular, the peak magnitude of $u'_p = 0.46$ was predicted to within 3% of the measured value as reported by Norberg (1998).

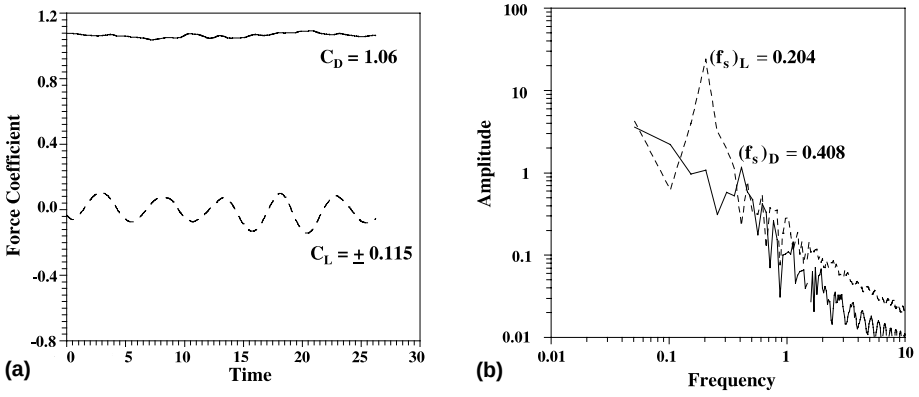

Fig. 4. Time history of the lift (C_L) and drag (C_D) coefficients and respective spectra amplitudes as predicted by the present LES computation. $(f_s)_L$ and $(f_s)_D$ denote the respective fundamental shedding frequency; (a) Lift and drag coefficients; (b) spectral amplitudes.

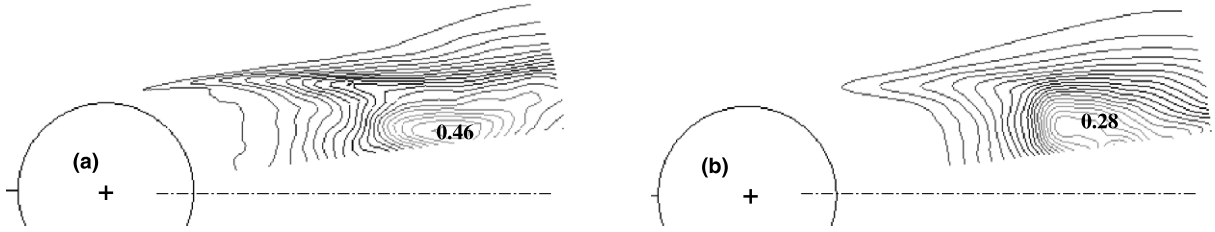

Fig. 5. Contours of the fluctuating: (a) Streamwise velocity (u'_{rms}, scaled by U) and (b) pressure coefficient (C'_p) as predicted by the present LES computation of cylinder near wake at $Re = 8000$. Contours (a) Max. 0.46, Min. 0.0, Incr. 0.023 and (b) Max. 0.28, Min. 0.0, Incr. 0.014.

4.2. Resolved local physics of the separated shear layer

Given the above validation, we can now begin investigating the transition process to turbulence for the $Re = 8000$ test case by re-examining the u'_{rms} contours in Fig. 5(a). One can see that this process begins near $x/D \sim 0.25$ as suggested by the lowest contour $u'_{rms} = 0.023$ – by comparison, Kourta et al. (1987) measured early signs of transition at $x/D = 0.5$ for $Re = 2400$ and $x/D = 0.45$ for $Re = 4500$. At this location, the shear-layer profiles of u' and the mean velocity ($\bar{u}$) are plotted in Fig. 6 where both quantities are spanwise averaged and re-scaled by the local shear-layer edge velocity (U_e). Clearly, the u' profile is symmetric and the inflexion point of $\bar{u}$ lies coincident with its respective maximum (u'_m), which is positioned at $y/D = 0.54$. Inasmuch as we expect the shear layer to initially destabilize at the inflexion point of $\bar{u}$, a time trace of u_m is shown in Fig. 7 slightly further downstream at $x/D = 0.32$. This figure plainly shows initial "transition waves" superimposed onto the fundamental oscillation. The exponential growth of u'_m as well as the growth of the mean momentum thickness (θ) and integrated kinetic energy (E^*_u) are illustrated in Fig. 8 where the latter property is evaluated across the shear layer according to

$$E^*_u = \left(\frac{1}{2}\int \frac{u'^2(y)}{U_e^2\theta_m}\mathrm{d}y\right)^{1/2}. \tag{11}$$

The momentum thickness (θ_m) in this equation is the characteristic length scale taken at the mid-point of the shear-layer exponential growth segment. The minor discontinuity in the growth rate of each property at $x/D \sim 1.5$ signifies that the transition process is complete. The time trace of u_m and its respective energy spectra at $x/D = 1.51$, plotted in Fig. 9, support this conclusion as seen by the random fluctuations in the time history and the distinct 5/3 s exponential decay in the energy spectrum.

This cursory analysis tell us that transition to turbulence at $Re = 8000$ occurs on the order of the cylinder diameter, beginning at $x/D \sim 0.25$ from the separation point. With this understanding, we can now explore the velocity spectra of u_m to gain further insight into the transition modes of the cylinder separated shear-layer. The velocity spectra of the time trace in Fig. 7 ($x/D = 0.32$) reveals two distinct peaks (Fig. 10(a)). The primary peak denotes the large-scale shedding frequency while the secondary one designates the Bloor frequency. Their ratio is $f_b/f_s = 9.4$. Further downstream at $x/D = 0.41$ (Fig. 10(b)), the spectral content of u_m shows its amplitude maturing at the Bloor frequency and the first appearance of a mixed mode $2f_b + 2f_s$. The spectral amplitude of the Kármán vortex remains unchanged as expected. Continuing downstream to $x/D = 0.52$ (Fig. 10(c)), the velocity spectra of u_m becomes much noisier at the higher modes. However, we can easily detect rising amplitudes at f_b and mode $2f_b + 2f_s$, and a broadband mode centered at $1/2f_b + 1/2f_s$. Still further downstream at $x/D = 0.61$ (Fig. 10(d)), the amplitude of

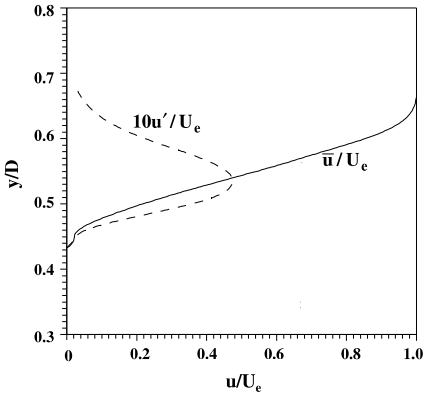

Fig. 6. Profiles of the mean ($\bar{u}$) and fluctuating (u') streamwise velocity (scaled by the edge velocity U_e) through the shear layer at $x/D = 0.25$.

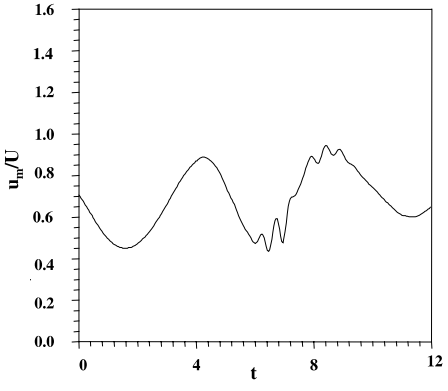

Fig. 7. Time trace of the spanwise-averaged streamwise velocity at $x/D = 0.32$ and $y/D = 0.54$.

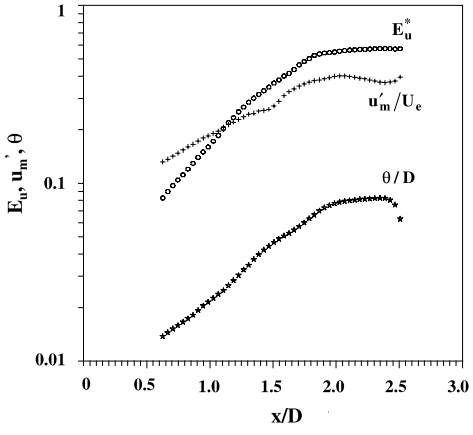

Fig. 8. Growth of several important parameters of the separated shear layer; see Fig. 2 for notation.

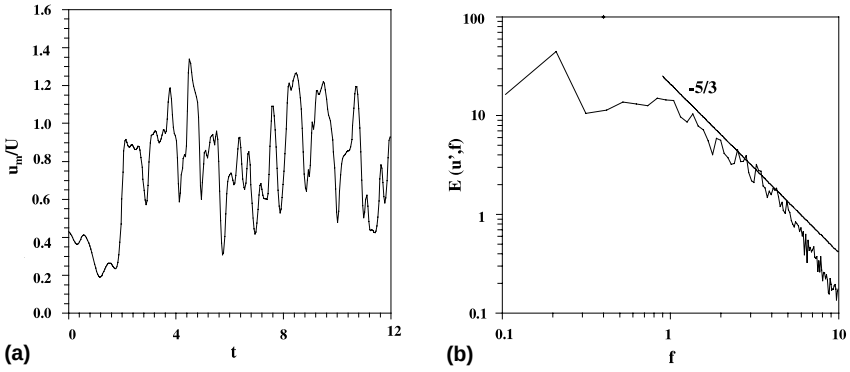

Fig. 9. (a) Time trace; (b) respective spectral energy of the streamwise velocity at $x/D = 1.51$.

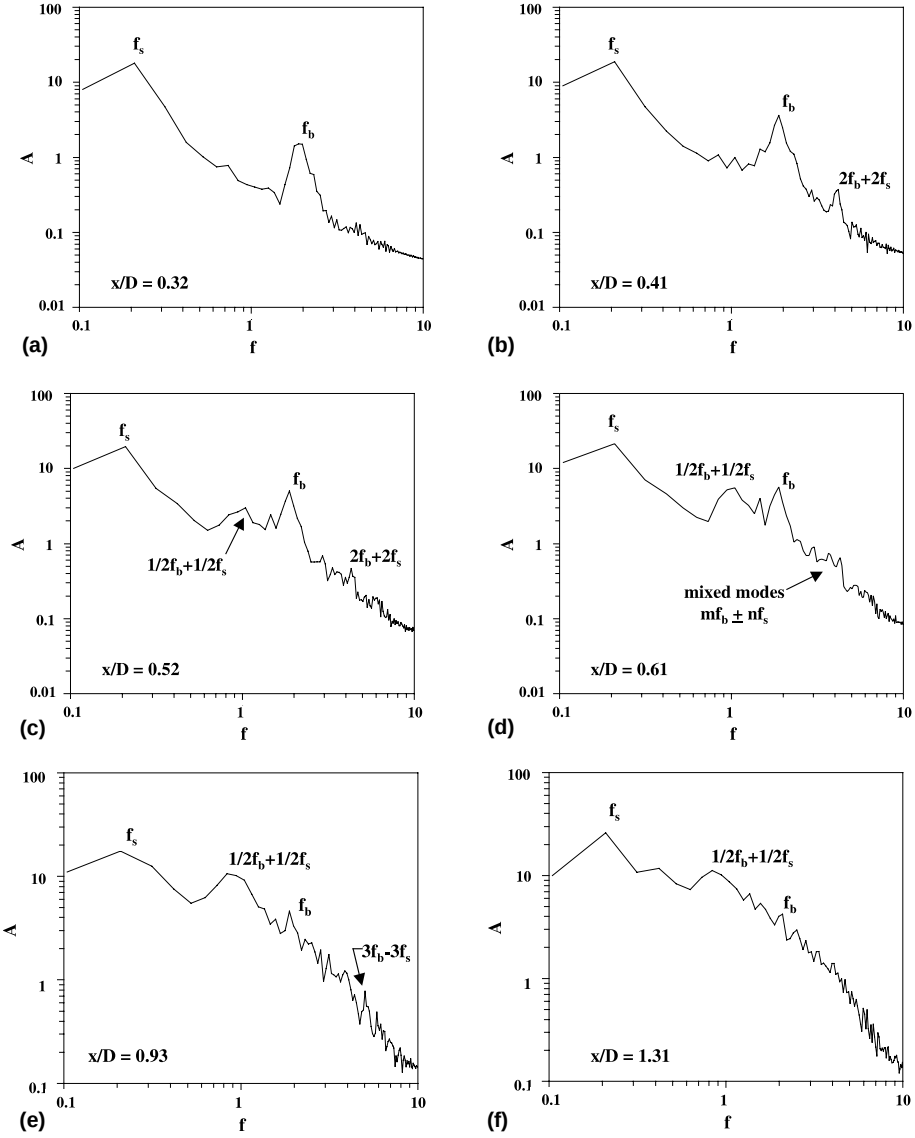

Fig. 10. Spanwise-averaged spectral amplitudes of the maximum streamwise velocity (u_m) inside the cylinder separated shear-layer at $Re = 8000$; x/D reference to mean separation point.

the latter mode doubles, but the Bloor frequency amplitude has leveled off. Several higher discrete modes are indicated in this figure, but only up to mode $2f_b + 2f_s$. One should note that the few mixed modes, as predicted by the present LES results, agrees with the spectral measurements observed in the upper limit of the low-*Re* range $(2000 < Re < 16,000)$ as reported by Kourta et al. (1987).

Beyond $x/D = 0.61$, the spectral profiles of u_m begin to take shape like that of a fully turbulent shear layer. For example, a 5/3 s exponential decay of the spectral amplitude is visible in Fig. 10(e) $(x/D = 0.93)$ that suggests the presence of an inertial sub-range. However, the Bloor frequency is still quite apparent in the figure. Its amplitude finally becomes nearly indistinguishable at $x/D = 1.31$ (Fig. 10(f)). These results agree essentially with the hot-wire anemometer measurements of Bloor (1964) and Schiller and Linke (1933). But their suggestion that transition is complete at $x/D \sim 0.75$ for this *Re* is somewhat premature according to the present computation. The present outcome also disputes the flow visualization observation by Szepessy (1994), who suggested that the spanwise transition line is about one diameter downstream from the cylinder center at this *Re*. Locating the precise disappearance of the Bloor "transition wave" in the shear layer is subjective. But as suggested by the spectral amplitudes of the maximum streamwise velocity component shown herein, the process leading to a fully turbulent shear layer begins at $x/D \sim 0.25$ and concludes after about one diameter.

A second and equally important purpose of the present computation is to investigate any character change of the shear layer with increasing Reynolds number. As noted earlier, Unal and Rockwell (1988) uncovered similar exponential growth rates of several shear-layer properties at specific Reynolds numbers; namely, $Re = 2500, 3400$ and 5040. Using their rational of scaling, the present results give the same rates as illustrated by the example in Fig. 11 for $E_u^*(\theta_m = 0.042)$. Moreover, Fig. 12 suggests that the growth rate of the momentum thickness during transition is linearly dependent on the Reynolds number. Besides studying their growth rates, Unal and Rockwell also showed an exponential increase in the magnitudes of the characteristic fluctuating velocities that strongly correlated with the base pressure coefficient. As illustrated in Fig. 13, their trends observed over $1900 < Re \leqslant 5040$ clearly hold true to $Re = 8000$ as extended by the present LES results.

One final argument that we can address by the present LES results is the higher frequency oscillation associated with the K–H vortices in the shear layer as determined by Wei and Smith (1986). In Fig. 14, the spanwise vorticity contours unmistakably trace the formation and growth of coherent structures inside the shear layer beyond $x/D = 0.5$. Like the observations of Wei and Smith, no signs of coalesce inside the shear layer was predicted by the computation. According to Wei and Smith, these structures fluctuate at frequency $f_i \sim 2.4$ Hz for the present *Re*. Unfortunately, the respective velocity spectra do not support this prediction. As previously discussed, the Bloor frequency distinctly

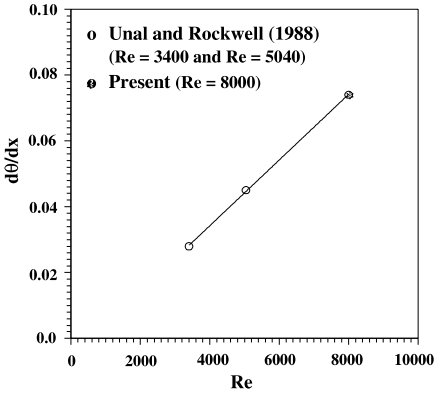

Fig. 12. Mean growth rate of the momentum thickness (θ) through the transition region of the separated shear layer.

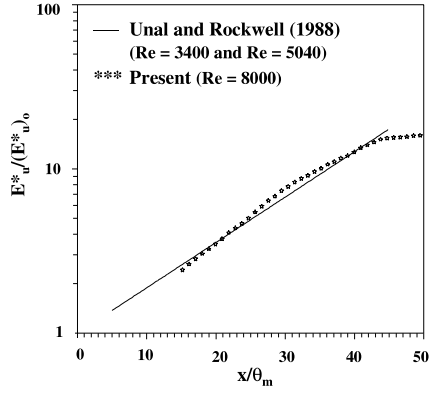

Fig. 11. Growth of the integrated kinetic energy (E_u^*) through the transition region of the separated shear layer.

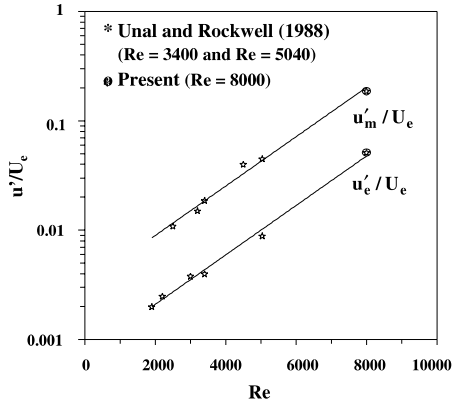

Fig. 13. Exponential variation of the maximum (u'_m) and edge (u'_e) streamwise fluctuations (normalized by the shear-layer edge velocity, (U_e) as a function of *Re*; $x/D = 0.5$.

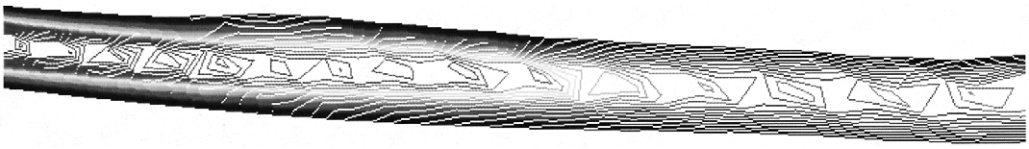

Fig. 14. Appearance of Kelvin–Helmholtz vortices in the separated shear layer at $Re = 8000$; spanwise vorticity contours Max. 30, Min. 10, Incr. 0.5.

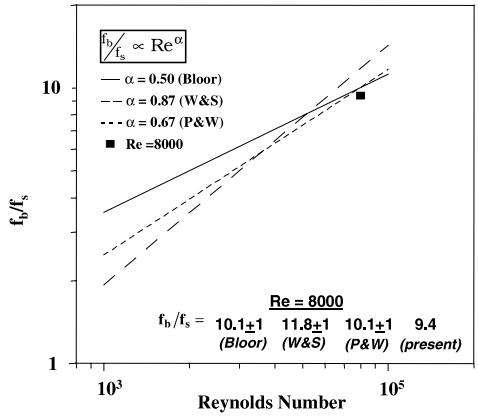

Fig. 15. Comparison of present frequency ratio (f_b/f_s) to published experimental data; Bloor (1964), W&S: Wei and Smith (1986), P&W: Prasad and Williamson (1996).

characterizes the predominant small-scale oscillation throughout the shear-layer transition process to turbulence. Although several higher mixed-modes are detectable (Fig. 10(d) for example), they are not indicative of the K–H instability waves seen by Wei and Smith. After comparing the LES prediction to the data collected by Prasad and Williamson (1996), their relationship $f_b/f_s = \kappa Re^{\beta}$, where $\kappa = 0.0235$ and $\beta = 0.6742$, appears satisfactory for estimating the frequency of the K–H vortices at least in the range of the present subcritical Reynolds number (see Fig. 15).

5. Concluding remarks

The large-eddy simulation methodology served as a suitable technique for resolving the shear-layer physics of the separated circular cylinder at $Re = 8000$. During the computation the dynamic SGS model, which usually plays an important role of representing the fine-scale turbulence physics at wavenumber cut-off, was not a major contributor to the predicted shear-layer characteristics. In the regions after turbulence transition in the shear layer, the frequency to wavenumber conversion (Choi and Moin, 1990) of the power spectra indicates that most of the equilibrium range was resolved by the grid spacing. Further downstream, the resolved–modeled field interactions were similar to that reported by Jordan and Ragab (1998) for their $Re = 5600$ computation.

Interestingly, the present computation did not predict the numerous modes ($mf_b \pm nf_s$) within the shear layer as reported by Braza et al. (1990) in their two-dimensional simulation at $Re = 3000, 5000$ and 10,000. Instead, only several mixed modes were present that agreed with the spectral measurements of the upper limit in the low-Re range as seen by Kourta et al. (1987). Furthermore, the K–H vortices did not coalesce prior to completion of the transition process. Bloor's frequency was clearly prevalent throughout the entire process with only two other distinct modes detectable at different locations within the shear layer. These waves were determined by averaging their amplitudes along the shear-layer span. A narrow-band higher mode ($2f_b + 2f_s$) appeared very early in the transition process with velocity amplitude equal to about half that of the Bloor "transition wave". While this wave was receding in amplitude further downstream in the shear layer, there appeared a second broadband mode ($1/2f_b + 1/2f_s$). This mode grew in amplitude to eventually bridge the gap in the development of the full turbulent energy spectra that was caused by separation of the fundamental frequencies of the large-scale vortex shedding and the shear-layer K–H vortices. The appearance and growth of this mode coincides with the small-scale structure observations by Wei and Smith (1986), but their associated frequencies at $Re = 8000$ are approximately 1/2 of mode $1/2f_b + 1/2f_s$.

Unal and Rockwell (1988) investigated several shear-layer properties that displayed self-similar growth rates throughout the transition region for tested Reynolds numbers ranging between 1900 and 5040. These properties include the maximum and edge velocity fluctuations, integrated kinetic energy and mean momentum thickness. An important outcome of the present computation at $Re = 8000$ is that the results showed identical self-similar growth rates of each characteristic. Finally, besides examining growth rates, Unal and Rockwell showed an exponential dependence on Reynolds number of the maximum and edge velocity fluctuations in the shear layer up to $Re = 5040$. The present results extend the validity of their relationships to $Re = 8000$.

Acknowledgements

The author gratefully acknowledges the support of the Office of Naval Research (Dr. L. Patrick Purtell,

Program Officer) and the In-House Independent Research Program (Mr. R. Philips, Coordinator) at the Naval Undersea Warfare Center Division Newport.

References

Bloor, M.S., 1964. The transition to turbulence in the wake of a circular cylinder. J. Fluid Mech. 19, 290.

Braza, M., Chassaing, P., Minh, H.H., 1990. Prediction of large-scale transition features in the wake of a circular cylinder. Phys. Fluids A 2, 1461–1470.

Braza, M., Persillon, H., Sers, F., 1993. Prediction of certain transition characteristics in the wake of a circular cylinder in free and forced flow. In: Eckelmann, , et al. (Eds.), IUTAM Symposium on Bluff-Body Wakes Dynamics and Instabilities. Springer, Berlin, pp. 279–284.

Cantwell, B., Coles, D., 1983. An experimental study of entrainment and transport in the turbulent near wake of a circular cylinder. J. Fluid Mech. 136, 321–374.

Choi, H., Moin, P., 1990. On the space-time characteristics of wall-pressure fluctuations. Phys. Fluids A 2 (8), 1450–1460.

Germano, M., 1992. Turbulence: the filtering approach. J. Fluid Mech. 238, 325–336.

Germano, M., Piomelli, U., Moin, P., Cabot, W.H., 1991. A dynamic subgrid-scale eddy viscosity model. Phys. Fluids A 3, 1760–1765.

Ho, C.M., Huerre, P., 1984. Perturbed free shear layers. Ann. Rev. Fluid Mech. 16, 365–424.

Jordan, S.A., 1999. A large-eddy simulation methodology in generalized curvilinear coordinates. J. Comput. Phys. 148, 322–340.

Jordan, S.A., 2001. Dynamic subgrid-scale modeling for large-eddy simulations in complex topologies. J. Fluids Eng. 123, 619–627.

Jordan, S.A., Ragab, S.A., 1996. An efficient fractional-step technique for unsteady incompressible flows using a semi-staggered grid strategy. J. Comput. Phys. 127, 218–225.

Jordan, S.A., Ragab, S.A., 1998. A large-eddy simulation of the near wake of a circular cylinder. J. Fluids Eng. 120, 243–252.

Kim, J., Moin, P., 1985. Application of a fractional-step method to incompressible Navier–Stokes equations. J. Comput. Phys. 59, 308–310.

Kourta, A., Boisson, H.C., Chassaing, P., Minh, H.H., 1987. Nonlinear interaction and the transition to turbulence in the wake of a circular cylinder. J. Fluid Mech. 181, 141–161.

Kravchenko, A.G., Moin, P., 2000. Numerical studies of flow over a circular cylinder at $Re_D = 3900$. Phys. Fluids 12 (2), 403–417.

Lilly, D.K., 1992. A proposed modification of the germano subgrid-scale closure method. Phys. Fluids A 4, 633–635.

Ma, X., Karamanos, G.S., Karnidakis, G.E., 2000. Dynamics and low-dimensionality of a turbulent near wake. J. Fluid Mech. 410, 29–65.

Mansy, H., Yang, P., Williams, D.R., 1994. Quantitative measurements of three-dimensional structures in the wake of a circular cylinder. J. Fluid Mech. 270, 277–296.

Mittal, R., Balachandar, S., 1996. Effect of three-dimensionality on the lift and drag of nominally two-dimensional cylinders. Phys. Fluids 7 (8), 1841–1865.

Norberg, C., 1993. Pressure forces on a circular cylinder in cross flow. In: IUTAM Symposium Bluff-Body Wakes Dynamics and Instabilities. Springer, Berlin, pp. 275–278.

Norberg, C., 1998. LDV-measurements in the near wake of a circular cylinder. ASME Fluids Engineering Division Summer Conference Paper FEDSM98-5202.

Prasad, A., Williamson, C.H.K., 1996. The instability of the separated shear layer from a bluff body. Phys. Fluids 8 (6), 1347–1349.

Roshko, A., 1976. Structure of turbulent shear flows: a new look. AIAA J. 14, 1349–1357.

Schiller, L., Linke, W., 1933. Z. Flugtech. Motorluft 24, 193.

Smagorinsky, J., 1963. General circulation experiments with the primitive equations I. The basic experiment. Mon. Weather Rev. 91, 99–164.

Son, J.S., Hanratty, T.J., 1969. Velocity gradients at the wall for flow around a cylinder at Reynolds numbers from 5×10^3 to 10^5. J. Fluid Mech., Part 2 35, 353–368.

Strouhal, V., 1878. Uber eine besondere Art der Tonerregung. Ann. Phys. Chemi, New Series 5, 216–251.

Szepessy, S., 1994. On the spanwise correlation of vortex shedding from a circular cylinder at high subcritical Reynolds number. Phys. Fluids 6 (7), 2408–2416.

Tadrist, H., Martin, R., Tadrist, L., Seguin, P., 1990. Experimental investigation of fluctuating forces exerted on a circular cylinder tube reynolds numbers from 3000 to 30,000. Phys. Fluids 2 (12), 2176–2182.

Unal, M.F., 1985. Vortex Formation from Bluff and Thin Trailing Edges. Ph.D. Dissertation, Lehigh University, Bethlehem, PA 18015.

Unal, M.F., Rockwell, D., 1988. On vortex formation from a cylinder. Part 1. The initial stability. J. Fluid Mech. 190, 491–512.

Wei, T., Smith, C.R., 1986. Secondary vortices in the wake of circular cylinders. J. Fluid Mech. 169, 513–533.

White, F.W., 1974. Viscous Fluid Flow. McGraw-Hill, New York.

Williamson, C.H., 1995. Vortex dynamics in the wake of a cylinder. In: Green, S.L. (Ed.), Fluid Vortices: Fluid Mechanics and Its Application, vol. 30. Kluwer Academic Publishers, Dordrecht, pp. 134–155.

Williamson, C.H.K., Wu, J., Sheridan, J., 1995. Scaling of the streamwise vortices in wakes. Phys. Fluids A 7, 112–122.